Dynamic magnonic crystals based on vanadium dioxide gratings

Aleksei A. Nikitin,* Andrey E. Komlev, Andrey A. Nikitin, Alexey B. Ustinov, and Erkki Lähderanta

Department of Physics, LUT University, 53850 Lappeenranta, Finland

(Received 11 July 2023; revised 14 August 2023; accepted 25 September 2023; published 10 October 2023)

The properties of spin-wave quanta, referred to as magnons, make them a promising signal carrier for the transmission and processing of information in magnetic materials. In this field, called magnonics, dynamic magnonic crystals attract special attention for applications such as complex real-time spectral transformations, due to on-demand controllability of transmission gaps. Here, we report on the experimental realization of the dynamic control of spin-wave band structures in artificial crystals using the metal-insulator transition in the vanadium dioxide (VO_2) grating. The obtained results are confirmed by a theoretical approach predicting a dramatic variation of the reflection coefficient from the VO_2 stripes upon the phase transition. The proposed structure combines the excellent versatility, fast switching speed, low power consumption, and external control it affords.

DOI: 10.1103/PhysRevApplied.20.044026

I. INTRODUCTION

The application of magnonic devices in wave-based computing systems shows the growing potential for efficient data transfer [1–6]. The key advantages offered by magnons are operation in the gigahertz (GHz) and terahertz frequency ranges, possibility to process data over a wide temperature range, access to pronounced nonlinear phenomena, and others. Despite these advantages, existing logic and computational magnonic devices still demonstrate lower efficiency and compactness in comparison with their electronic counterparts based on the complementary metal oxide semiconductor (CMOS) architecture. There are a number of problems that need to be solved before magnonic logic devices will be able to compete with CMOS-based circuits, including cumbersome Oe-field tuning or subampere-current control. At the same time, scientific and technological challenges in the field of magnonics are being extensively investigated, and many proof-of-concept prototypes have already been realized. Nowadays, various concepts for interfacing magnonics with CMOS are available that simplify integration into hybrid systems. Magnon spintronics [7], magnetoelectric [8], magnetoacoustic [9], and magneto-optical [10] solutions are able to substitute the classical approach based on Oersted fields, which have poor scaling behavior.

Other challenges associated with the implementation of magnonic devices exploiting quanta of spin waves (SWs) are related to the appropriate choice of waveguide material and structure. Yttrium iron garnet (YIG) is the traditional material for magnonics, owing to its physical properties: low magnetic damping for propagating SWs, wide tunability of dispersion properties, and a variety of nonlinear effects [11,12]. Regarding the waveguide structure, artificial magnetic media with periodically modulated properties, known as magnonic crystals, possess great potential for signal-processing applications [13–19]. Their promising functionality arises from band-structure engineering that is mainly caused by spin-wave Bragg reflections from periodic disturbances. In YIG-based magnonic crystals, these disturbances are produced by periodic variations of thickness [20,21], width [22,23], magnetization [24,25], and metallization [26,27]. However, the band structure of these crystals is predetermined during fabrication and cannot be easily modified without invoking structural changes in the system. This restriction is resolved by exploiting a waveguide structure with rapidly switchable periodic properties, known as a dynamic magnonic crystal (DMC) [28].

The intensive development of magnonics inspired a range of DMCs based on different physical mechanisms [29–36]. Among others, periodic metallization of a magnetic film surface is one of the conventional methods. The general idea of this approach involves the influence of conductive planes on spin-wave propagation in ferrite films [37–42]. Spin-wave transmission in the YIG/metal bilayer strongly depends on the metal thickness, its conductivity, and the distance between layers. Dynamic control of one of these parameters naturally realizes the essential ingredients for a DMC. This concept can be implemented by using transition-metal oxides due to the mechanism of a metal-insulator transition (MIT).

Among various materials that undergo a prominent MIT phenomenon, vanadium dioxide (VO_2) is an advanced

*aleksei.a.nikitin@gmail.com

functional material with wide applications due to its physical properties [43,44]. Nowadays, VO_2 films are utilized in Mott field-effect transistors [45], nanophotonics [46], neuromorphic devices [47], spintronic applications [48,49], etc. Strong interest is focused on an abrupt change of the conductivity near the VO_2 phase-transition temperature (around 340 K). In principle, such a transition can be triggered on ultrafast timescales using different stimuli: thermal [50], electrical [51,52], optical [53], or external stress [54]. Recent advances in the fabrication of magnonic structures and correlated oxide-based films constitute an essential milestone for cutting-edge interdisciplinary expertise in magnonics and electronics. This topic has special potential, considering recent theoretical progress linking the SW dynamics of ferrite films to the MIT properties of VO_2 [55,56]. Following this idea, the proof of concept of the control of microwave spin-wave dynamics in YIG/VO_2 bilayers was reported on the microscale and nanoscale [57,58]. In contrast to earlier works that focused on investigations of the direct impact of the MIT on spin-wave dynamics, we demonstrate a variable reflection coefficient for surface SWs from a VO_2 stripe. This phenomenon provides an alternative mechanism for the dynamic control of magnonic band structures in ferrite films.

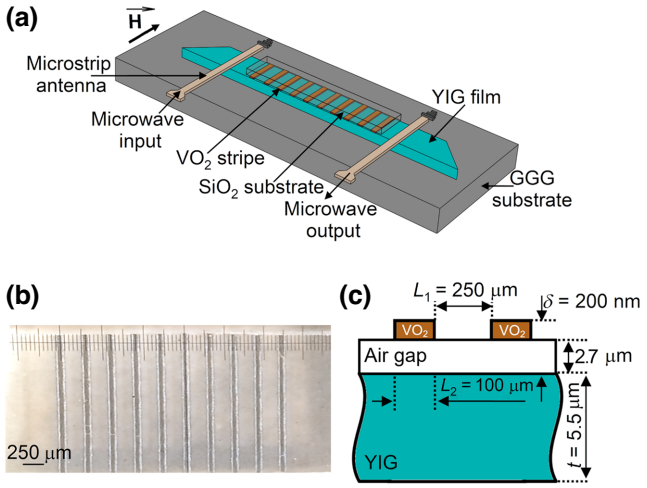

FIG. 1. (a) DMC with two 50-μm-wide microwave antennas for excitation and reception of surface spin waves in an in-plane magnetized layered structure. Antennas are patterned on top of the YIG film at a distance of 7.3 mm away from each other. DMC consists of 5.5-μm-thick YIG film on GGG substrate and physically separated 200-nm-thick vanadium dioxide (VO_2) stripes with a width of $L_2 = 100$ μm at a distance of $L_1 = 250$ μm. (b) Photograph of the VO_2 grating deposited on the amorphous quartz (SiO_2) substrate. (c) Cross section of a DMC fragment.

II. DESIGN OF THE DYNAMIC MAGNONIC CRYSTAL

The investigated device is fabricated in the form of a phase shifter. Figure 1(a) illustrates the structure comprising the YIG film, the attached VO_2 grating, and microstrip antennas. The DMC itself is part of the YIG waveguide contacted with the VO_2 stripes. A photograph of the fabricated VO_2 grating is shown in Fig. 1(b).

The experimental structure is prepared by means of a two-step technique. The first step is the fabrication of a YIG film with a thickness of $t = 5.5$ μm grown by liquid-phase epitaxy on a gadolinium gallium garnet (GGG) substrate. The spin-wave waveguide was cut from the YIG/GGG wafer in the form of a 3-cm-long and 2-mm-wide stripe. Both edges of the stripe were cut at an angle of 45° to prevent spin-wave reflections during microwave measurements. The sample has a ferromagnetic resonance linewidth of $\Delta H = 0.6$ Oe at a frequency of 5 GHz and saturation magnetization of $4\pi M_s = 1820$ G at room temperature that was verified by a local nondestructive technique, known as a "magnetic well" [59]. To accomplish the effective excitation and reception of SWs in the structure, short-circuited microstrip antennas with a width of 50 μm and a length of 2.5 mm are used. The antennas are positioned at the top surface of the YIG film at a distance of 7.3 mm away from each other and fed by microstrip transmission lines of 50-Ω characteristic impedance. The measurement cell is magnetized by a uniform magnetic field of $H = 1175$ Oe applied across the YIG waveguide along the antennas to provide the conditions for the excitation of surface SWs.

The second step is the fabrication of the VO_2 grating. First, a VO_2 film with a thickness of $\delta = 200$ nm is deposited on the amorphous quartz (SiO_2) substrate by reactive dc magnetron sputtering under an argon and oxygen atmosphere. The film deposition time was 30 min, while the target-substrate distance was 80 mm. The sample had in-plane dimensions of 4×2 mm^2. Then the stripes of the VO_2 grating were produced from the deposed film by the laser ablation technique. To accomplish this, a high-power ytterbium fiber laser with a precise galvanometric scanning module was used. The laser operated in a pulse regime with a repetition rate of 50 kHz, pulse duration of 100 ns, spot diameter of 100 μm, and peak power of 50 μJ. As shown in Fig. 1(a), the design of the periodic structure consists of ten parallel VO_2 stripes with a width of $L_2 = 100$ μm spaced by $L_1 = 250$ μm. Thus, the lattice constant is $\Lambda = L_2 + L_1 = 350$ μm. Finally, to implement the DMC, the VO_2 grating is pressed on top of the YIG film so that the stripes are located on its surface [see Fig. 1(a)]. As shown in Fig. 1(c), a thin air gap between the VO_2 grating and YIG film exists due to imperfections located at the edges of the VO_2 stripes. The profile of the stripes is investigated and discussed in detail in Sec. III.

III. CHARACTERIZATION OF THE VO_2 GRATING

The operating principle of the studied device is based on the transformation of the spin-wave dispersion spectrum, which occurs due to a prominent change in the VO_2 conductivity. To study the properties of the VO_2 grating, we examined the structural properties, phase-transition mechanism, and surface profile. Figure 2(a) shows the x-ray diffraction pattern of the deposited film, where an insulating monoclinic phase of vanadium dioxide with (110) orientation in the region of $2\theta = 28°$ is detected. Figure 2(b) illustrates temperature dependences of the VO_2 conductivity. Here, a sharp change in conductivity from 1.35 to 1980 S/cm is observed in the temperature range from 315 to 345 K with both heating (red squares) and cooling (blue circles). This process is associated with a first-order phase transition caused by the transformation of a monoclinic VO_2 crystal structure into a tetragonal one.

We use atomic force microscopy to further examine the geometry of the VO_2 stripes. Figure 3 presents a typical morphology measured at area of $100 \times 100\,\mu m^2$ surrounding a stripe edge. The white dashed line in Fig. 3(a) shows the path where a surface profile is examined. As can be seen, both surfaces of the VO_2 film and amorphous quartz substrate are almost homogeneous within the regions marked I and III, while imperfections are concentrated along the edges of the VO_2 stripe corresponding to region II. This region has a width of $L_d = 30$ μm and consists of defects with the shape of vertical flakes and tips measuring up to 2.7 μm in height [see Fig. 3(b)]. These defects are formed during the ablation process, which causes a deformation of the surface of the melt and its intensive outflow from the affected area is probably accompanied by splashing. Owing to these effects, the oxygen concentration in region II can vary over a wide range, suppressing the MIT nature of VO_2 stripes [60–62]. Note that these imperfections also provide the gap between the grating and the surface of the YIG film. This gap is considered to be a low-conductive layer with a thickness of 2.7 μm [see Fig. 1(c)]. According to our estimates, the introduction of a thin low-conductive layer between the YIG and VO_2 films has a negligible impact on the spin-wave dynamics in the GHz frequency range.

IV. THEORETICAL APPROACH

The propagation character of SWs is of crucial importance for magnonic crystals, since the band structure is mainly caused by the destructive interference of incident waves and those reflected by the grating. To get a deeper insight into the MIT-induced reflection mechanism, the problem of SW scattering from VO_2 stripes can be posed as an integral-equation formulation of the problem, similar to the phenomenological approach developed in Ref. [63]. In that work, the authors derived the following equation to describe reflections of surface SWs in a ferrite film with thickness t from a perfectly conductive stripe with width w:

$$\Gamma \approx j\pi w^2 (K_2 - K_2^*) \frac{\sinh(K_2^* t)}{\sinh(K_2 t)} \frac{\mu_{xx} - j\mu_{xy}}{1 - j\mu_{xy} + \mu_{xx}} \times \frac{0.25 + \beta^2}{\cosh(\pi\beta)} \frac{1 - e^{-2K_2 t}}{4t} \sqrt{\frac{(1+\mu_{xx})^2 + \mu_{xy}^2}{\mu_{xx}^2 + \mu_{xy}^2}}, \quad (1)$$

where K_2 and K_2^* are wave numbers of surface SWs propagating in the forward and backward directions, respectively, in the metal-coated ferrite film; $\beta = \frac{1}{2\pi}\ln\left[\frac{1-j\mu_{xy}+\mu_{xx}}{1+j\mu_{xy}+\mu_{xx}}\frac{\mu_{xx}+j\mu_{xy}}{\mu_{xx}-j\mu_{xy}}\right]$; and μ_{xx} and μ_{xy} are the elements of the magnetic permeability tensor of the ferrite layer. To apply this approach to a magnetic structure covered by a VO_2 stripe with finite conductivity, in Eq. (1) we substitute the complex wave numbers k_2 and k_2^* for K_2 and K_2^*, as well as δ and L_2 for t and w. Both complex wave numbers can be obtained at the same carrier frequency, $\omega = 2\pi f$, using the theory presented in our earlier work [55]. Recently, a similar model was used to describe low-loss spin-wave propagation in YIG/Pt bilayers covered by a ground plate [41]. Moreover, we use the elements of the permeability tensors written in a complex form:

$$\mu_{xx} = 1 + \frac{(\omega_H + j\omega\alpha)\omega_M}{(\omega_H + j\omega\alpha)^2 - \omega^2}; \mu_{xy} = \frac{\omega\omega_M}{(\omega_H + j\omega\alpha)^2 - \omega^2}.$$

Here, $\omega_H = 2\pi|\gamma|H$; $\alpha = \Delta H/H$; $\omega_M = 2\pi|\gamma|4\pi M_s$, where $|\gamma| = 2.8$ MHz/Oe is the gyromagnetic ratio; and ΔH is the ferromagnetic resonance linewidth.

The derived relationship was used to analyze the variation of the reflection coefficient for different values of VO_2 conductivity obtained from the experimentally determined dependences [see Fig. 2(b)]. The corresponding calculations were carried out for parameters of the structure, as outlined in Fig. 1(c). The result of modeling is shown in Fig. 4. Here, the SW carrier frequency was normalized by a cutoff frequency for the surface SW, $f_\perp = \sqrt{\omega_H(\omega_H + \omega_M)}/2\pi$, to distinguish the influence of temperature on the ferrite magnetic properties from the direct impact of the MIT.

As seen in Fig. 4, the VO_2 stripe exhibiting an insulator state ($\sigma = 60$ S/cm) provides a low power-reflection coefficient ($|\Gamma|^2 < 0.001$) in the experimental frequency range. In this case, only up to 0.1% of the incident SW energy is reflected due to the low impedance mismatch between the waveguide sections. It means that the array of VO_2 stripes has a negligible effect on the scattering of SWs. A rapid change in the VO_2 conductivity up to 1600 S/cm provides an increase of the power-reflection coefficient from 0.001 to 0.137 at $1.018 f_\perp$. This process is of crucial importance to predict the SW band structure.

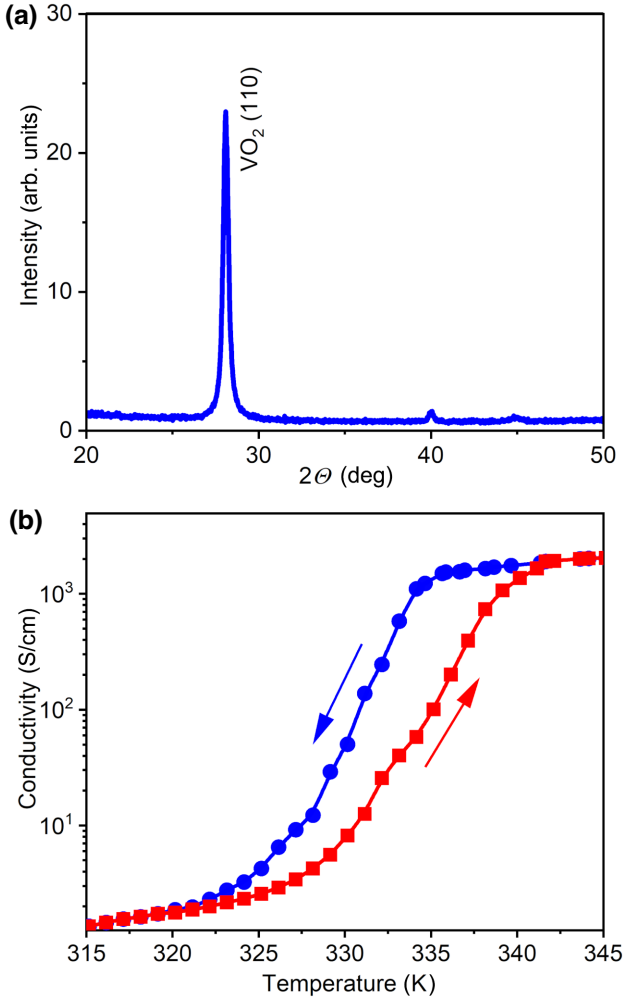

FIG. 2. (a) X-ray diffraction pattern of the vanadium dioxide (VO_2) sample deposited on the amorphous quartz substrate. (b) Temperature dependences of the VO_2 conductivity, showing a metal-insulator transition between 315 and 345 K. Measured results are shown by red and blue symbols attributed to heating and cooling semicycles, respectively.

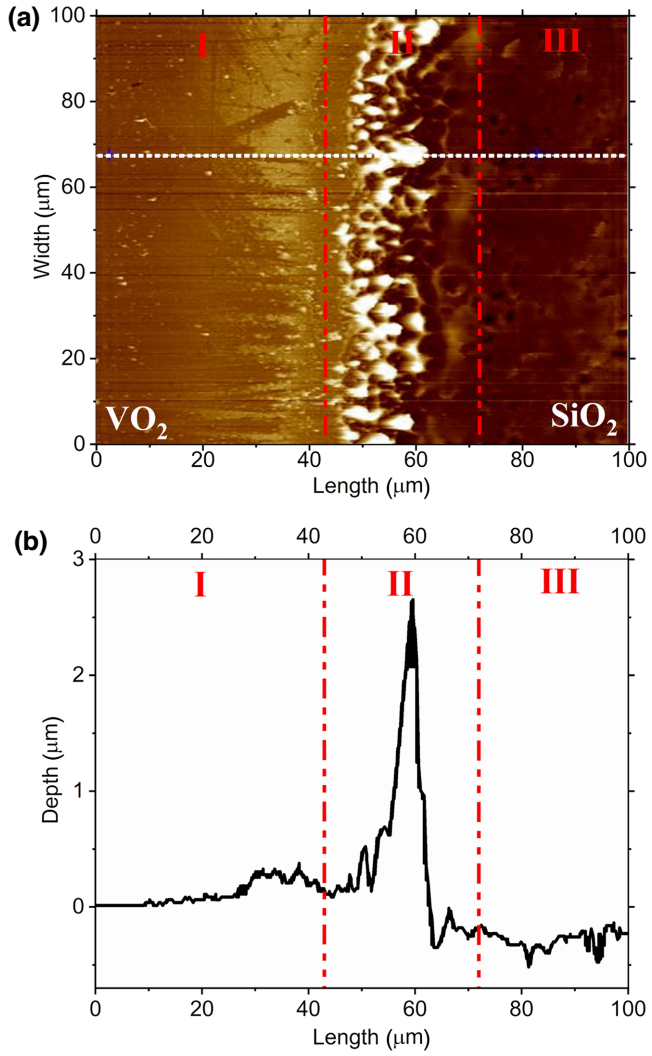

FIG. 3. (a) Atomic force microscopy image of the VO_2 grating. Almost homogeneous regions I and III correspond to surfaces of VO_2 and SiO_2, respectively, while region II, highlighted by red dashed lines, represents imperfections along the edges of the VO_2 stripe. (b) Surface profile measured at the path marked by the white dotted line in (a).

Following the nature of the Bragg resonance, the formation of transmission gaps, referred to as rejection bands, is due to multiple reflections from the edges of all stripes, which form partial standing waves in the space between the VO_2 stripes. The effect of a set of the stripes is obtained by cascading the structural periods using the transfer-matrix method. According to this, matrices $\mathbf{T}^{(1)}$ and $\mathbf{T}^{(3)}$ were used to describe the surface SW propagation in the uncovered YIG film and YIG/VO_2 bilayer, respectively. These matrices have diagonal components only: $\mathbf{T}^{(1)}_{11} = 1/\ \mathbf{T}^{(1)}_{22} = \exp(-j\,k_1 L_1)$; $\mathbf{T}^{(3)}_{11} = \exp(-j\,k_2 L_2)$; $\mathbf{T}^{(3)}_{22} = \exp(jk^*_2 L_2)$. Here, k_1, k_2, and k^*_2 are complex wave numbers of the surface SWs propagating in the uncovered YIG film, YIG/VO_2 bilayer in the forward and backward directions, respectively. Matrices $\mathbf{T}^{(2)}$ and $\mathbf{T}^{(4)}$ described reflections of the surface SWs from the front and rear edges of the VO_2 stripe, respectively. As shown in Fig. 4, the reflection coefficient of a single stripe strongly depends on the VO_2 conductivity. Considering that the derived reflection coefficient at the edges of a VO_2 stripe is $|\Gamma|$, and the transmission through the junction is $1-|\Gamma|$, the matrices are given by $\mathbf{T}^{(2)}_{11} = \mathbf{T}^{(2)}_{22} = 1/(1-|\Gamma|)$, $\mathbf{T}^{(2)}_{12} = \mathbf{T}^{(2)}_{21} = |\Gamma|/(1-|\Gamma|)$, $\mathbf{T}^{(4)}_{11} = \mathbf{T}^{(4)}_{22} = 1/(1+|\Gamma|)$, and $\mathbf{T}^{(4)}_{12} = \mathbf{T}^{(4)}_{21} = -|\Gamma|/(1+|\Gamma|)$. The final transfer matrix for the ferrite film with the VO_2 grating formed by $N=10$ stripes is obtained by multiplying all $\mathbf{T}$ matrices as follows: $\mathbf{T}_\Sigma = (\mathbf{T}^{(1)} \cdot \mathbf{T}^{(2)} \cdot \mathbf{T}^{(3)} \cdot \mathbf{T}^{(4)})^N$. Therefore, the complex transfer function for the spatially

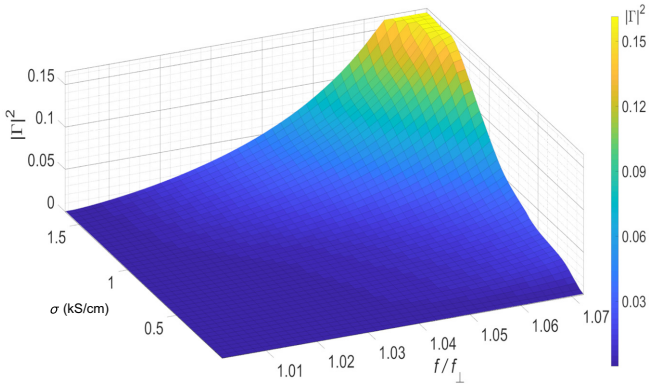

FIG. 4. Color-mapped surface of the power-reflection coefficient for surface spin waves in the ferrite film from the VO_2 stripe versus frequency obtained for various conductivities across the metal-insulator transition. Coloring is proportional to the calculated reflection coefficient indicated by the color bar.

periodic structure is equal to $1/\mathbf{T}_{\Sigma 11}$, and the power-transmission characteristic of the considered structure is given by $S_{21} = 20\log_{10}(1/|\mathbf{T}_{\Sigma 11}|)$. As a result, this approach allows one to calculate the transmission characteristics of the proposed DMC.

V. DYNAMIC CONTROL OF MAGNONIC BAND STRUCTURE

Consider now the propagation of the spin wave in the MIT-induced DMC. To this end, we carried out both theoretical and experimental investigations. In the experiments, we used a vector network analyzer (R&S®ZVA40) to measure the transmission characteristics of the DMC placed in a temperature-controlled probe station. Following the nature of the MIT hysteresis, we restrict ourselves to investigate only the transmission characteristics for the heating semicycle. The results are presented in Fig. 5. Here, experimental and theoretical transmission characteristics of the DMC are presented by black solid and red dashed lines, respectively. Note that additional dips existing in the experimental transmission characteristics near room temperature are formed due to standing spin-wave resonances appearing in the YIG film with pinned surface spins [64].

During modeling, we found out that the best possible fit between theoretical and experimental data was achieved when the stripe width was reduced by twice the defective region width, so that $L_2^*{=}L_2 - 2L_d$. The most probable reason for that is the disturbance of the VO_2 film's stoichiometry due to high thermal treatment after grating production. As mentioned above, the width of the defect regions, L_d, is equal to 30 μm at each side of the VO_2 stripes. In this case, the stripe width, L_2^*, is equal to 40 μm, while the period of the grating, $\Lambda = 350$ μm, remains the same. An additional small deviation between theoretical and experimental data is explained by the existence of other sources of insertion losses, such as mismatch losses, microstrip antenna impedance mismatches, and weak random inhomogeneity in the waveguide.

Next, we discuss the MIT-induced control of the band structure presented in Fig. 5. Near room temperature, the conductivity of the VO_2 grating is low [see Fig. 2(b)]. The insulating stripes have a negligible effect on spin-wave propagation, resulting in the absence of any periodic properties in the structure. To demonstrate this, the transmission characteristics of the free-standing YIG film and the YIG film covered by the VO_2 grating were measured at room temperature. The results are shown in Fig. 5(a) by black solid and blue dashed-dotted lines, respectively. As seen in this figure, the loss slowly increases from a minimum value of 17 dB to about 45 dB for both structures.

Heating of the DMC provides the transition of the VO_2 grating to an intermediate state. Namely, the variation of temperature within a narrow range from 336 to 339 K provides a sharp increase in VO_2 conductivity from 240 to 1050 S/cm. As presented in Figs. 5(b)–5(d), the impact of the grating on the DMC performance characteristics is enhanced by heating. While the band structure in Fig. 5(b) is not practically visible in the transmission characteristic measured at 336 K, the depths of the rejection bands become more pronounced for the DMC heated to 339 K [see Fig. 5(d)]. This occurs mainly due to an increase of the reflection coefficient. At the same time, insertion losses introduced by the grating are enhanced and result in narrowing of the bandwidth from $0.062f_\perp$ to $0.05f_\perp$, as shown in Figs. 5(b) and 5(d), respectively.

As seen in Fig. 5(e), the impact of the grating on the SW transmission becomes stronger at 341 K, where the VO_2 conductivity is 1670 S/cm. In contrast to the previous case of 339 K, the DMC bandwidth narrows to $0.027f_\perp$. Following conventional Bragg analysis, the first two rejection bands are formed at frequencies of $1.009f_\perp$ and $1.018f_\perp$, while the third one is not observed in the experiment due to its frequency position near the border of the bandwidth. The depth of the first rejection band is 2 dB. This value is caused by a weak reflection of the SWs from the VO_2 stripes ($|\Gamma|^2 = 6.4 \times 10^{-3}$). Numerical calculation predicts the rise of the reflection coefficient with frequency, resulting in more pronounced high-order rejection bands [see Fig. 4]. Indeed, the depth of the second rejection band significantly increases. Note that this rejection band demonstrates the greatest depth over the entire temperature range studied. This is because lower temperature provides weak SW reflections, while higher temperature leads to a suppression of high-order rejection bands.

To demonstrate this suppression, we heated the structure to 343 K, where the conductivity of the VO_2 stripes was equal to 1925 S/cm. As presented in Fig. 5(f), the

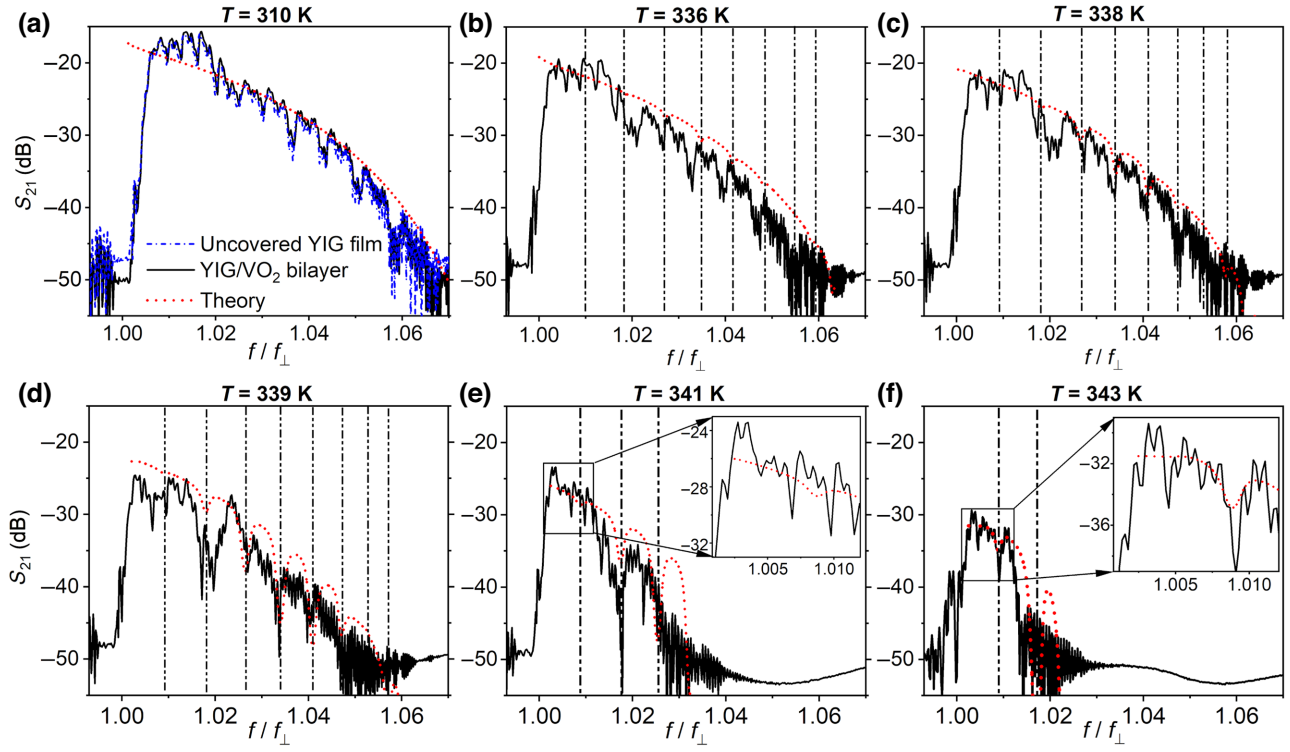

FIG. 5. Transmission characteristics of the dynamic magnonic crystal for six temperatures of (a) 310 K, (b) 336 K, (c) 338 K (d) 339 K, (e) 341 K, and (f) 343 K. Here, black solid curves represent experimental characteristics, while red dashed lines show, for comparison, results of the theoretical analysis. Black dashed-dotted vertical lines show the frequencies that correspond to the wave numbers satisfying the Bragg reflection.

grating strongly affects the spin-wave dynamics. This effect can be described as follows. First, the transmission characteristic is suppressed by 12 dB in comparison with the uncovered YIG waveguide, and its bandwidth is narrowed to $0.014f_{\perp}$. This behavior is determined by an increase in the insertion losses introduced by the conducting grating. Second, a single rejection band at a frequency of $1.009f_{\perp}$ is formed within the bandwidth of the structure. Other rejection bands are formed outside the transmission characteristic and do not appear in the experiment. The depth of the first rejection band is 4 dB, which is more pronounced than the one in the previous case of 341 K. This difference is caused by increasing conductivity resulting in a higher reflection coefficient.

VI. FINAL REMARKS AND CONCLUSIONS

To fully exploit the potential of the proposed concept for practical applications, the device sizes and the method to induce the MIT phenomenon have to be optimized. Miniaturization of the magnetic waveguide can be realized by using the latest generation of YIG films of submicron thicknesses fabricated by using various techniques [65–67]. The low energy consumption of DMCs and minimal activation time of a magnonic band structure can be achieved by using an electrical-induced MIT instead of by adjusting the temperature. To demonstrate this, we performed additional measurements showing the principle of spin-wave control by a direct current through a 500-nm-thick VO_2 stripe placed on the surface of a 5.7-μm-thick YIG film with a saturation magnetization of 1750 G. We fabricated VO_2 and YIG samples by the same approach, as described in Sec. II. The measurement cell was magnetized by a uniform magnetic field of $H = 1175$ Oe applied across the YIG waveguide and the VO_2 stripe connecting to the Keithley 2410 source meter. To prevent the scattering of spin waves from a thin nonmagnetic wire carrying a dc current, an external resistor of resistance $R_E = 8$ kΩ was added to the electrical circuit between the power supply and VO_2 stripe. The application of a direct current of 14 mA to the stripe induces an abrupt increase in VO_2 conductivity, which governs the increase of insertion loss and leads to narrowing of the transmission band to 260 MHz. This behavior is similar to the results obtained by adjusting the temperature, as presented in Fig. 5. Accordingly, the spin-wave transmission can be effectively changed by varying the direct current to a maximum value of 14 mA applied to the VO_2 stripe. In contrast, current control of the magnetic Oersted field produced by a wire or a set of wires in logic devices [68] and in DMCs [28] requires

more than 1.2 and 0.5 A, respectively. Moreover, the activation time of the magnonic band structure in the proposed current-controlled device depends mainly on the switching time between insulating and conducting states in a VO_2 stripe. For an electrical-induced MIT, this time is in the order of nanoseconds [69], which is comparable to existing current-controlled magnonic crystals. A detailed study of the effect of the electrical-induced MIT on spin-wave dynamics falls outside of the scope of this manuscript. However, we believe that it deserves to be the subject of another research paper, and we sincerely hope that our paper will become a trigger for such studies.

In summary, the proposed DMC offers promising features, such as alternative mechanisms for engineering of the band structure, low energy consumption, and ultrafast switching times. In addition, these crystals are compatible with conventional magnonic devices enabling enhanced logic functionality. Thus, the considered structures look favorable for applications as a complimentary part to the traditional approach for general computing and microwave signal processing.

ACKNOWLEDGMENTS

This work was supported by the INERCOM platform of LUT University.

[1] M. Krawczyk and D. Grundler, Review and prospects of magnonic crystals and devices with reprogrammable band structure, J. Phys.: Condens. Matter **26**, 123202 (2014).

[2] S. A. Nikitov, D. V. Kalyabin, I. V. Lisenko, A. N. Slavin, Yu. N. Barabanenkov, S. A. Osokin, A. V. Sadovnikov, E. N. Beginin, M. A. Morozova, Yu. P. Sharaevsky, *et al.*, Magnonics: A new research area in spintronics and spin wave electronics, Phys.-Usp. **58**, 1002 (2015).

[3] G. Csaba, Á Papp, and W. Porod, Perspectives of using spin waves for computing and signal processing, Phys. Lett. A **381**, 1471 (2017).

[4] A. Barman, G. Gubbiotti, S. Ladak, A. O. Adeyeye, M. Krawczyk, J. Gräfe, C. Adelmann, S. Cotofana, A. Naeemi, V. I. Vasyuchka, *et al.*, The 2021 magnonics roadmap, J. Phys.: Condens. Matter **33**, 413001 (2021).

[5] P. Pirro, V. I. Vasyuchka, A. A. Serga, and B. Hillebrands, Advances in coherent magnonics, Nat. Rev. Mater. **6**, 1 (2021).

[6] A. V. Chumak, P. Kabos, M. Wu, C. Abert, C. Adelmann, A. O. Adeyeye, J. Åkerman, F. G. Aliev, A. Anane, A. Awad, *et al.*, Advances in magnetics roadmap on spin-wave computing, IEEE Trans. Magn. **58**, 1 (2022).

[7] A. V. Chumak, V. I. Vasyuchka, A. A. Serga, and B. Hillebrands, Magnon spintronics, Nat. Phys. **11**, 453 (2015).

[8] B. Rana and Y. Otani, Towards magnonic devices based on voltage-controlled magnetic anisotropy, Commun. Phys. **2**, 90 (2019).

[9] I. Lisenkov, A. Jander, and P. Dhagat, Magnetoelastic parametric instabilities of localized spin waves induced by traveling elastic waves, Phys. Rev. B **99**, 184433 (2019).

[10] S. Schlauderer, C. Lange, S. Baierl, T. Ebnet, C. P. Schmid, D. C. Valovcin, A. K. Zvezdin, A. V. Kimel, R. V. Mikhaylovskiy, and R. Huber, Temporal and spectral fingerprints of ultrafast all-coherent spin switching, Nature **569**, 383 (2019).

[11] B. A. Kalinikos and A. B. Ustinov, Nonlinear spin waves in magnetic films and structures: Physics and devices, Solid State Phys. **64**, 193 (2013).

[12] V. V. Vitko, A. A. Nikitin, R. V. Haponchyk, A. A. Stashkevich, M. P. Kostylev, and A. B. Ustinov, Bistable behavior of active ring resonator on surface spin waves, Eur. Phys. J. Plus **137**, 1010 (2022).

[13] A. B. Ustinov, A. V. Drozdovskii, and B. A. Kalinikos, Multifunctional nonlinear magnonic devices for microwave signal processing, Appl. Phys. Lett. **96**, 142513 (2010).

[14] M. Inoue, A. Baryshev, H. Takagi, P. B. Lim, K. Hatafuku, J. Noda, and K. Togo, Investigating the use of magnonic crystals as extremely sensitive magnetic field sensors at room temperature, Appl. Phys. Lett. **98**, 132511 (2011).

[15] M. A. Morozova, S. V. Grishin, A. V. Sadovnikov, Y. P. Sharaevskii, and S. A. Nikitov, Magnonic bandgap control in coupled magnonic crystals, IEEE Trans. Magn. **50**, 1 (2014).

[16] E. Bankowski, T. Meitzler, R. S. Khymyn, V. S. Tiberkevich, A. N. Slavin, and H. X. Tang, Magnonic crystal as a delay line for low-noise auto-oscillators, Appl. Phys. Lett. **107**, 122409 (2015).

[17] P. J. Metaxas, M. Sushruth, R. A. Begley, J. Ding, R. C. Woodward, I. S. Maksymov, M. Albert, W. Wang, H. Fangohr, A. O. Adeyeye, and M. Kostylev, Sensing magnetic nanoparticles using nano-confined ferromagnetic resonances in a magnonic crystal, Appl. Phys. Lett. **106**, 232406 (2015).

[18] A. V. Chumak, A. A. Serga, and B. Hillebrands, Magnonic crystals for data processing, J. Phys. D: Appl. Phys. **50**, 244001 (2017).

[19] A. A. Nikitin, A. A. Nikitin, A. B. Ustinov, E. Lähderanta, and B. A. Kalinikos, Theory of spin-electromagnetic waves in planar thin-film multiferroic heterostructures based on a coplanar transmission line and its application for electromagnonic crystals, IEEE Trans. Magn. **54**, 1 (2018).

[20] Y. Zhu, K. H. Chi, and C. S. Tsai, Magnonic crystals-based tunable microwave phase shifters, Appl. Phys. Lett. **105**, 022411 (2014).

[21] A. A. Nikitin, A. A. Nikitin, I. L. Mylnikov, A. B. Ustinov, and B. A. Kalinikos, Electromagnonic crystals based on ferrite-ferroelectric-ferrite multilayers, IET Microwaves Antennas Propag. **14**, 1304 (2020).

[22] P. Frey, A. A. Nikitin, D. A. Bozhko, S. A. Bunyaev, G. N. Kakazei, A. B. Ustinov, B. A. Kalinikos, F. Ciubotaru, A. V. Chumak, Q. Wang, and V. S. Tiberkevich, Reflectionless width-modulated magnonic crystal, Commun. Phys. **3**, 17 (2020).

[23] H. Merbouche, M. Collet, M. Evelt, V. E. Demidov, J. L. Prieto, M. Muñoz, J. B. Youssef, G. de Loubens, O. Klein, S. Xavier, *et al.*, Frequency filtering with a magnonic crystal based on nanometer-thick yttrium iron garnet films, ACS Appl. Nano Mater. **4**, 121 (2021).

[24] F. Ciubotaru, A. V. Chumak, B. Obry, A. A. Serga, and B. Hillebrands, Magnonic band gaps in waveguides with a periodic variation of the saturation magnetization, Phys. Rev. B **88**, 134406 (2013).

[25] H. Qin, G. J. Both, S. J. Hämäläinen, L. Yao, and S. van Dijken, Low-loss YIG based magnonic crystals with large tunable bandgaps, Nat. Commun. **9**, 5445 (2018).

[26] V. D. Bessonov, M. Mruczkiewicz, R. Gieniusz, U. Guzowska, A. Maziewski, A. I. Stognij, and M. Krawczyk, Magnonic band gaps in YIG-based one-dimensional magnonic crystals: An array of grooves versus an array of metallic stripes, Phys. Rev. B **91**, 104421 (2015).

[27] N. Kanazawa, T. Goto, J. W. Hoong, A. Buyandalai, H. Takagi, and M. Inoue, Metal thickness dependence on spin wave propagation in magnonic crystal using yttrium iron garnet, J. Appl. Phys. **117**, 17E510 (2015).

[28] A. V. Chumak, T. Neumann, A. A. Serga, B. Hillebrands, and M. P. Kostylev, A current-controlled, dynamic magnonic crystal, J. Phys. D: Appl. Phys. **42**, 205005 (2009).

[29] A. V. Chumak, V. S. Tiberkevich, A. D. Karenowska, A. A. Serga, J. F. Gregg, A. N. Slavin, and B. Hillebrands, All-linear time reversal by a dynamic artificial crystal, Nat. Commun. **1**, 141 (2010).

[30] A. A. Nikitin, A. B. Ustinov, A. A. Semenov, A. V. Chumak, A. A. Serga, V. I. Vasyuchka, E. Lähderanta, B. A. Kalinikos, and B. Hillebrands, A spin-wave logic gate based on a width-modulated dynamic magnonic crystal, Appl. Phys. Lett. **106**, 102405 (2015).

[31] M. Vogel, A. V. Chumak, E. H. Waller, T. Langner, V. I. Vasyuchka, B. Hillebrands, and G. Von Freymann, Optically reconfigurable magnetic materials, Nat. Phys. **11**, 487 (2015).

[32] Q. Wang, A. V. Chumak, L. Jin, H. Zhang, B. Hillebrands, and Z. Zhong, Voltage-controlled nanoscale reconfigurable magnonic crystal, Phys. Rev. B **95**, 134433 (2017).

[33] B. Rana and Y. Otani, Voltage-controlled reconfigurable spin-wave nanochannels and logic devices, Phys. Rev. Appl. **9**, 014033 (2018).

[34] S. Choudhury, A. K. Chaurasiya, A. K. Mondal, B. Rana, K. Miura, H. Takahashi, Y. Otani, and A. Barman, Voltage controlled on-demand magnonic nanochannels, Sci. Adv. **6**, eaba5457 (2020).

[35] A. B. Ustinov, A. V. Drozdovskii, A. A. Nikitin, A. A. Semenov, D. A. Bozhko, A. A. Serga, B. Hillebrands, E. Lähderanta, and B. A. Kalinikos, Dynamic electromagnonic crystal based on artificial multiferroic heterostructure, Commun. Phys. **2**, 137 (2019).

[36] R. G. Kryshtal and A. V. Medved, Surface acoustic waves in dynamic magnonic crystals for microwave signals processing, Ultrasonics **94**, 60 (2019).

[37] A. G. Veselov, S. L. Vysotskiy, G. T. Kazakov, A. G. Sukharev, and Y. A. Filimonov, Surface magnetostatic waves in metal-plated yttrium iron garnet films, J. Commun. Technol. Electron. **39**, 102 (1994).

[38] Y. Zhang, D. Cai, C. Zhao, M. Zhu, Y. Gao, Y. Chen, X. Liang, H. Chen, J. Wang, Y. Wei, and Y. He, Nonreciprocal isolating bandpass filter with enhanced isolation using metallized ferrite, IEEE Trans. Microwaves Theory Tech. **68**, 5307 (2020).

[39] S. Mae, R. Ohshima, E. Shigematsu, Y. Ando, T. Shinjo, and M. Shiraishi, Influence of adjacent metal films on magnon propagation in $Y_3Fe_5O_{12}$, Phys. Rev. B **105**, 104415 (2022).

[40] A. Krysztofik, N. Kuznetsov, H. Qin, L. Flajšman, E. Coy, and S. van Dijken, Tuning of magnetic damping in $Y_3Fe_5O_{12}$/metal bilayers for spin-wave conduit termination, Materials **15**, 2814 (2022).

[41] R. O. Serha, D. A. Bozhko, M. Agrawal, R. V. Verba, M. Kostylev, V. I. Vasyuchka, B. Hillebrands, and A. A. Serga, Low-damping spin-wave transmission in YIG/Pt-interfaced structures, Adv. Mater. Interfaces **9**, 2201323 (2022).

[42] J. Xu, Z. Liao, Q. Wang, B. Liu, X. Tang, Z. Zhong, L. Zhang, Y. Zhang, H. Zhang, and L. Jin, Enhancement of low-k spin-wave transmission efficiency with a record-high group velocity in YIG/nonmagnetic metal heterojunctions, Adv. Electron. Mater. **9**, 2201061 (2022).

[43] K. Liu, S. Lee, S. Yang, O. Delaire, and J. Wu, Recent progresses on physics and applications of vanadium dioxide, Mater. Today **21**, 875 (2018).

[44] R. Shi, N. Shen, J. Wang, W. Wang, A. Amini, N. Wang, and C. Cheng, Recent advances in fabrication strategies, phase transition modulation, and advanced applications of vanadium dioxide, Appl. Phys. Rev. **6**, 011312 (2019).

[45] D. Ruzmetov, G. Gopalakrishnan, C. Ko, V. Narayanamurti, and S. Ramanathan, Three-terminal field effect devices utilizing thin film vanadium oxide as the channel layer, J. Appl. Phys. **107**, 114516 (2010).

[46] S. Cueff, J. John, Z. Zhang, J. Parra, J. Sun, R. Orobtchouk, S. Ramanathan, and P. Sanchis, VO_2 nanophotonics, APL Photonics **5**, 110901 (2020).

[47] Y. Zhou and S. Ramanathan, Mott memory and neuromorphic devices, Proc. IEEE **103**, 1289 (2015).

[48] K. Tamura, T. Kanki, S. Shirai, H. Tanaka, Y. Teki, and E. Shikoh, Spin injection into vanadium dioxide films from a typical ferromagnetic metal, across the metal–insulator transition of the vanadium dioxide films, AIP Adv. **11**, 035120 (2021).

[49] J. Y. Kim, J. Cramer, K. Lee, D. S. Han, D. Go, P. Salev, P. N. Lapa, N. M. Vargas, I. K. Schuller, Y. Mokrousov, and G. Jakob, Tuning spin-orbit torques across the phase transition in VO_2/NiFe heterostructure, Adv. Funct. Mater. **32**, 2111555 (2022).

[50] J. Lappalainen and M. Kangaspuoskari, Interface effects of strain-energy potentials on phase transition characteristics of VO_2 thin-films, ACS Omega **8**, 21083 (2023).

[51] Y. Zhou, X. Chen, C. Ko, Z. Yang, C. Mouli, and S. Ramanathan, Voltage-triggered ultrafast phase transition in vanadium dioxide switches, IEEE Electron Device Lett. **34**, 220 (2013).

[52] N. V. Andreeva, P. A. Turalchuk, D. A. Chigirev, I. B. Vendik, E. A. Ryndin, and V. V. Luchinin, Electron impact processes in voltage-controlled phase transition in vanadium dioxide thin films, Chaos, Solitons Fractals **142**, 110503 (2021).

[53] A. X. Gray, M. C. Hoffmann, J. Jeong, N. P. Aetukuri, D. Zhu, H. Y. Hwang, N. C. Brandt, H. Wen, A. J. Sternbach, S. Bonetti, and A. H. Reid, Ultrafast terahertz field control of electronic and structural interactions in vanadium dioxide, Phys. Rev. B **98**, 045104 (2018).

[54] J. Cao, E. Ertekin, V. Srinivasan, W. Fan, S. Huang, H. Zheng, J. W. L. Yim, D. R. Khanal, D. F. Ogletree, J. C. Grossman, and J. Wu, Strain engineering and one-dimensional organization of metal-insulator domains in single-crystal vanadium dioxide beams, Nat. Nanotechnol. **4**, 732 (2009).

[55] A. A. Nikitin, V. V. Vitko, A. A. Nikitin, A. B. Ustinov, V. V. Karzin, A. E. Komlev, B. A. Kalinikos, and E. Lähderanta, Spin-wave phase shifters utilizing metal–insulator transition, IEEE Magn. Lett. **9**, 1 (2018).

[56] A. A. Nikitin, V. V. Vitko, A. A. Nikitin, A. B. Ustinov, and B. A. Kalinikos, Microwave tunable devices on the YIG-VO_2 structures, J. Phys.: Conf. Ser. **1400**, 044001 (2019).

[57] A. A. Nikitin, A. A. Nikitin, A. B. Ustinov, A. E. Komlev, E. Lähderanta, and B. A. Kalinikos, Metal–insulator switching of vanadium dioxide for controlling spin-wave dynamics in magnonic crystals, J. Appl. Phys. **128**, 183902 (2020).

[58] T. S. Safi, P. Zhang, Y. Fan, Z. Guo, J. Han, E. R. Rosenberg, C. Ross, Y. Tserkovnyak, and L. Liu, Variable spin-charge conversion across metal-insulator transition, Nat. Commun. **11**, 1 (2020).

[59] B. A. Kalinikos, N. G. Kovshikov, P. A. Kolodin, and I. P. Panchurin, Frequency dependence of magnetic dissipation in microwave garnet films, IEEE Trans. Magn. **53**, 0700202 (2017).

[60] S. Shin, S. Suga, M. Taniguchi, M. Fujisawa, H. Kanzaki, A. Fujimori, H. Daimon, Y. Ueda, K. Kosuge, and S. Kachi, Vacuum-ultraviolet reflectance and photoemission study of the metal-insulator phase transitions in VO_2, V_6O_{13}, and V_2O_3, Phys. Rev. B **41**, 4993 (1990).

[61] D. H. Kim and H. S. Kwok, Pulsed laser deposition of VO_2 thin films, Appl. Phys. Lett. **65**, 3188 (1994).

[62] W. Yin, K. G. West, J. W. Lu, Y. Pei, S. A. Wolf, P. Reinke, and Y. Sun, The metal-insulator transition in vanadium dioxide: A view at bulk and surface contributions for thin films and the effect of annealing, J. Appl. Phys. **105**, 114322 (2009).

[63] V. A. Vugal'ter and V. N. Makhalin, Reflection and excitation of surface magnetostatic waves of the metal plane, Zh. Tekh. Fiz. **55**, 497 (1985).

[64] B. A. Kalinikos and A. N. Slavin, Theory of dipole-exchange spin wave spectrum for ferromagnetic films with mixed exchange boundary conditions, J. Phys. C: Solid State Phys. **19**, 7013 (1986).

[65] L. Soumah, N. Beaulieu, L. Qassym, C. Carrétéro, E. Jacquet, R. Lebourgeois, J. Ben Youssef, P. Bortolotti, V. Cros, and A. Anane, Ultra-low damping insulating magnetic thin films get perpendicular, Nat. Commun. **9**, 1505 (2018).

[66] C. Dubs, O. Surzhenko, R. Thomas, J. Osten, T. Schneider, K. Lenz, J. Grenzer, R. Hübner, and E. Wendler, Low damping and microstructural perfection of sub-40 nm-thin yttrium iron garnet films grown by liquid phase epitaxy, Phys. Rev. Mater. **4**, 024416 (2020).

[67] M. Lammel, D. Scheffler, D. Pohl, P. Swekis, S. Reitzig, S. Piontek, H. Reichlova, R. Schlitz, K. Geishendorf, L. Siegl, and B. Rellinghaus, Atomic layer deposition of yttrium iron garnet thin films, Phys. Rev. Mater. **6**, 044411 (2022).

[68] T. Schneider, A. A. Serga, B. Leven, B. Hillebrands, R. L. Stamps, and M. P. Kostylev, Realization of spin-wave logic gates, Appl. Phys. Lett. **92**, 022505 (2008).

[69] Z. Yang, C. Ko, and S. Ramanathan, Oxide electronics utilizing ultrafast metal-insulator transitions, Annu. Rev. Mater. Sci. **41**, 337 (2011).